

# The formation of Mg-orthocarbonate through the reaction $\text{MgCO}_3 + \text{MgO} = \text{Mg}_2\text{CO}_4$ at Earth's lower mantle $P$ – $T$ conditions

Pavel N. Gavryushkin <sup>\*1,2</sup>, Dinara N. Sagatova<sup>1,2</sup>, Nursultan Sagatov<sup>1</sup>, and Konstantin D. Litasov<sup>3</sup>

<sup>1</sup>*Sobolev Institute of Geology and Mineralogy, Siberian Branch of Russian Academy of Sciences, prosp. acad. Koptiyuga 3, 630090 Novosibirsk, Russia*

<sup>2</sup>*Novosibirsk State University, Pirogova 2, Novosibirsk 630090, Russia*

<sup>3</sup>*Vereshchagin Institute for High Pressure Physics RAS, 108840, Troitsk, Moscow, Russian Federation*

## Abstract

Orthocarbonates of alkaline earth metals are the newly discovered class of compounds stabilized at high pressures. Mg-orthocarbonates are the potential carbon host phases, transferring oxidized carbon in the Earth's lower mantle up to the core-mantle boundary. Here, we demonstrate the possibility for the formation of  $\text{Mg}_2\text{CO}_4$  in the lower mantle at pressures above 50 GPa, by *ab initio* calculations.  $\text{Mg}_2\text{CO}_4$  is formed by the reaction  $\text{MgCO}_3 + \text{MgO} = \text{Mg}_2\text{CO}_4$ , proceeding only at high-temperatures. At 50 GPa the reaction starts at 2200 K. The temperature decreases with pressure and drops down to 1085 K at the pressure of the Earth's core-mantle boundary, near 140 GPa. Two stable structures,  $\text{Mg}_2\text{CO}_4$ -*Pnma* and  $\text{Mg}_2\text{CO}_4$ -*P2<sub>1</sub>/c*, were revealed using crystal structure prediction technique.  $\text{Mg}_2\text{CO}_4$ -*Pnma* is isostructural to mineral forsterite ( $\text{Mg}_2\text{SiO}_4$ ), while  $\text{Mg}_2\text{CO}_4$ -*P2<sub>1</sub>/c* is isostructural to mineral larnite ( $\beta$ - $\text{Ca}_2\text{SiO}_4$ ). Transition pressure from  $\text{Mg}_2\text{CO}_4$ -*Pnma* to  $\text{Mg}_2\text{CO}_4$ -*P2<sub>1</sub>/c* is around 80 GPa. Both phases are dynamically stable on decompression down to the ambient pressure and can be preserved in the samples of natural high-pressure rocks or the products of experiments.  $\text{Mg}_2\text{CO}_4$ -*Pnma* has a melting temperature more than 16% higher than the melting temperature of magnesite ( $\text{MgCO}_3$ ). At 23.7 GPa, 35.5 GPa, and 52.2 GPa,  $\text{Mg}_2\text{CO}_4$ -*Pnma* melts at 2661 K, 2819 K, and 3109 K, respectively.

---

\*Electronic address: gavryushkin@igm.nsc.ru, p.gavryushkin@g.nsu.ru; Corresponding author

Acoustic wave velocities  $V_p$  and  $V_s$  of  $\text{Mg}_2\text{CO}_4\text{-}Pnma$  are very similar to that of magnesite, while universal anisotropy of  $\text{Mg}_2\text{CO}_4\text{-}Pnma$  is stronger than that of magnesite, as well as coefficient  $A^U$  is larger for orthocarbonate. Calculated Raman spectra of  $\text{Mg}_2\text{CO}_4\text{-}Pnma$  will help its identification in high pressure experiments.

## Introduction

During the recent decade, the crystal structure prediction technique became an integral part of high-pressure research. Numerous experimental synthesis were guided by this technique, for instance, the synthesis of the high-pressure phases of alkaline [1–3] and alkaline earth carbonates [4–10]. Orthocarbonates of alkaline earth metals are another example for experimental confirmation of theoretically predicted structures.

For a long time, Mg-orthocarbonate attracted attention of the Earth scientists as the possible phase of the deep Earth’s interiors. To the best of our knowledge, Fyfe was the first, who suggested the formation of  $\text{Mg}_2\text{CO}_4$  phase with spinel structure through the reaction  $\text{MgCO}_3 + \text{MgO} = \text{Mg}_2\text{CO}_4$  [11]. Then, the possibility of this reaction has been hypothesized by Irwing and Wyllie [12], and by Katsura [13]. However, recently performed *ab initio* crystal structure prediction calculations have not found any structures of  $\text{Mg}_2\text{CO}_4$  stable at pressures of the Earth’s mantle [14]. The enthalpies of all the found structures were lower than the enthalpy of the mechanical mixture of  $\text{MgCO}_3 + \text{MgO}$ , i.e. they were thermodynamically unstable.

Our calculations on crystal structure prediction have revealed stable crystal structures of Ca-, Sr-, and -Ba, orthocarboates,  $\text{Ca}_2\text{CO}_4$  [15],  $\text{Sr}_2\text{CO}_4$  [16], and  $\text{Ba}_2\text{CO}_4$  [16]. Subsequent experimental synthesis have confirmed the existence of  $\text{Ca}_2\text{CO}_4$  and  $\text{Sr}_2\text{CO}_4$  [17, 18], and  $\text{Mg}_2\text{CO}_4$  remains the sole representative of alkaline earth orthocarbonates for which stable structures are not yet known.

In the present work, we continue our investigation of orthocarbonates, find stable structures of  $\text{Mg}_2\text{CO}_4$ , calculate their melting temperatures, seismic properties and  $P$ – $T$  phase diagram, as well as Raman spectra for the identification in high-pressure experiments, which are currently underway.

## Methods

To increase the chances for finding the energetically favorable structures we have used both USPEX and AIRSS methods, each of which has apparent advantages [19]. *Ab initio* structure prediction was complemented by the prediction technique based on the known structures of Mg- and Zn- orthosilicates with isolated  $[\text{SiO}_4]$  tetrahedrons, as well as sulfates with isolated  $[\text{SO}_4]$  tetrahedrons.  $\text{Mg}_2\text{CO}_4$  structures were produced from these structures by the corresponding replacement of the cations and consequent local optimizations. The following crystal structures have been used (numbers in parentheses indicate the number of formula units (f.u.) in the unit cell): ringwodite ( $\text{Mg}_2\text{SiO}_4\text{-}Fd\bar{3}m$

(8)) [20], porierite ( $\text{Mg}_2\text{SiO}_4$ -*Pmma* (4)) [21], wadsleyite ( $\text{Mg}_2\text{SiO}_4$ -*Imma* (8)) [22], forsterite ( $\text{Mg}_2\text{SiO}_4$ -*Pnma* (4)) [23],  $\text{Zn}_2\text{SiO}_4$ -*Pbca* (8) [20],  $\text{Zn}_2\text{SiO}_4$ -*I42d* (4) [20],  $\text{Na}_2\text{SO}_4$ -*Fddd* (8) [24],  $\text{Li}_2\text{SO}_4$ -*P2<sub>1</sub>/c* (4) [25], and  $\text{Ca}_2\text{CO}_4$ -*Pnma* (4) [15].

The calculations with the USPEX method [26–29] have been performed for 1–4 f.u. of  $\text{Mg}_2\text{CO}_4$  at 25, 50, and 100 GPa. The seeding technique, implemented in version 10.2 of the USPEX, has been employed in all calculations. The aforementioned structures based on silicates, sulfates, and orthocarbonate have been used as the seeds. Totally, around 3000 structures have been calculated at each pressure. Crystal structure prediction with AIRSS 0.9.1 [30, 31] has been performed only at 50 GPa for 2, 3, and 4 f.u. and a total of nearly 4000 structures have been generated in this calculation.

The energetic optimizations of the predicted structures have been performed within density functional theory (DFT), implemented in the VASP package [32, 33].

To take into account the temperature effect and calculate  $P$ - $T$  phase diagram, we used the lattice dynamics method within the quasi-harmonic approximation (QHA). For this task, the lattice vibration frequencies were calculated with the PHONOPY code [34]. By our experience with  $P$ - $T$  phase diagrams of carbonates, this technique reliably reproduces phase boundaries in the wide temperature range [2, 15, 35], up to 80–90 % of the melting temperature, if the process of dynamical disordering does not take place.

Melting temperatures of the predicted structures have been determined, using the so-called *Z-method*, based on the molecular dynamic (MD) simulations [36].

To determine the wave velocities  $V_p$  and  $V_s$  and assess anisotropy of Mg-orthocarbonates, static elastic stiffness tensor ( $C_{ij}$ ) was calculated from the stress ( $\sigma$ )- strain ( $\epsilon$ ) relation  $\sigma_i = C_{ij}\epsilon_j$ . Based on these  $C_{ij}$  data, we calculated averages of bulk ( $B$ ) and shear ( $G$ ) moduli using the Voigt-Ruess-Hill scheme [37, 38]. Then we have determined compression ( $A_B$ ), shear ( $A_G$ ), and universal anisotropy ( $A^U$ ) indexes.

The details of DFT, crystal structure predictions, thermodynamic and elastic property calculations, and MD simulations are given in *Supporting information*.

In order to obtain the Raman spectra, the polarizability tensors for each crystal mode were calculated using the *vasp\_raman.py* code [39]. The atomic charges were analyzed by the grid-based bader analysis algorithm [40, 41], in which the grid is obtained by decomposition of the charge density by the static self-consistent calculation for the optimized structures. FindSym program [42] and instruments of Phonopy package have been used for the symmetry determination. VESTA and ToposPro [43, 44] programs have been used for the visualization of the crystal structures and figures preparation. The topology of the structures were analysed with ToposPro and Robocrystallographer programs [44, 45].

## Results and discussion

### Predicted structures

In the crystal structure prediction calculations at 25 and 50 GPa, USPEX has revealed the  $\text{Mg}_2\text{CO}_4$ - $Pnma$  structure as the most energetically favorable. This structure has lower enthalpy than  $\text{Mg}_2\text{CO}_4$ - $Cm$ , predicted by AIRSS, and structures, obtained based on the crystal structures of silicates and sulfates (Figure 1 and S1).

At 100 GPa, USPEX has found another favorable structure with monoclinic symmetry,  $\text{Mg}_2\text{CO}_4$ - $P2_1/c$ . The transition from  $\text{Mg}_2\text{CO}_4$ - $Pnma$  to  $\text{Mg}_2\text{CO}_4$ - $P2_1/c$  occurs at 52 GPa, and at higher pressures  $\text{Mg}_2\text{CO}_4$ - $P2_1/c$  is the most energetically favorable among considered structures (Figure 1 and Figure S1).

Other structures constructed based on the polymorphs of  $\text{Mg}_2\text{SiO}_4$ , ringwoodite, wadsleyite, and poirierite, do not have pressure ranges of stability. However, in the stability field of  $\text{Mg}_2\text{CO}_4$ - $P2_1/c$ , the series of phase transitions, forsterite  $\rightarrow$  poirierite  $\rightarrow$  wadsleyite  $\rightarrow$  ringwoodite, is realized on compression. Similar transitions are well known for  $\text{Mg}_2\text{SiO}_4$  system ([46] and references therein).

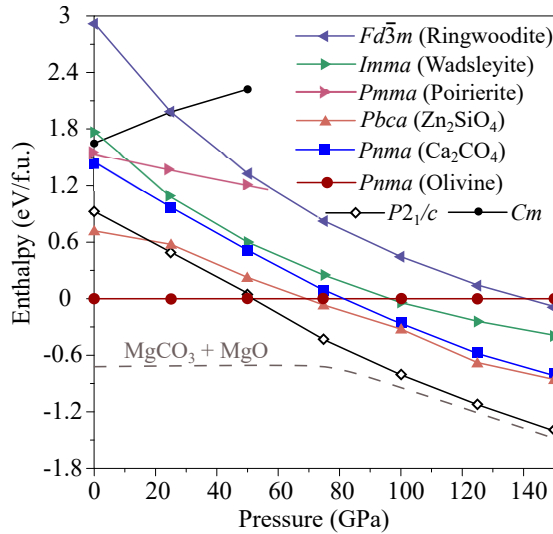


Figure 1: Enthalpy-pressure dependencies of  $\text{Mg}_2\text{CO}_4$  structures. Isostructural compounds are indicated in brackets.

Revealed  $\text{Mg}_2\text{CO}_4$ - $Pnma$  is isostructural to the mineral forsterite (Figure 2a,b). Atoms in both positions Mg(1) and Mg(2) are 6-coordinated, with the octahedral coordination polyhedron (Figure 2c).  $\text{Mg}_2\text{CO}_4$ - $P2_1/c$  is isostructural to  $\beta$ - $\text{Ca}_2\text{SiO}_4$  (larnite) and can be considered as the monoclinic analogue of  $\text{Ca}_2\text{CO}_4$ - $Pnma$ . In the crystal structure of  $\text{Mg}_2\text{CO}_4$ - $P2_1/c$ , there are also two non-equivalent Mg sites. There is some ambiguity in the determination of

coordination numbers of Mg atoms, due to the smooth variation of the bond lengths. In the first site, Mg(1) is bonded to six oxygen atoms, arranged in a highly deformed trigonal prism (Figure 2d). Lengths of the six Mg–O bonds within coordination polyhedron vary in the range 1.832–2.073 Å, while the seventh oxygen atom is distant on 2.382 Å. In the second site, Mg(2) is bonded to eight oxygen atoms, forming relatively regular square antiprism. Lengths of these eight Mg–O bonds vary in the range of 1.887–2.126 Å, while the ninth Mg–O bond is significantly longer, being equal to 2.688 Å. For comparison, in  $\text{Mg}_2\text{CO}_4\text{-}Pnma$  structure, oxygen atoms in the first coordination sphere is distant on 1.815–1.888 Å for Mg(1) site and on 1.781–1.95 Å — for Mg(2) site. All the presented bond lengths correspond to the pressure of 100 GPa. In both  $Pnma$  and  $P2_1/c$  crystal structures, coordination polyhedrons around Mg atoms share both vertices and edges with  $[\text{CO}_4]$  tetrahedrons (Figure 2c,d). Transition from  $\text{Mg}_2\text{CO}_4\text{-}Pnma$  to  $\text{Mg}_2\text{CO}_4\text{-}P2_1/c$  is accompanied by the sufficient decrease of the volume equal to 5.7 % (Figure S2).

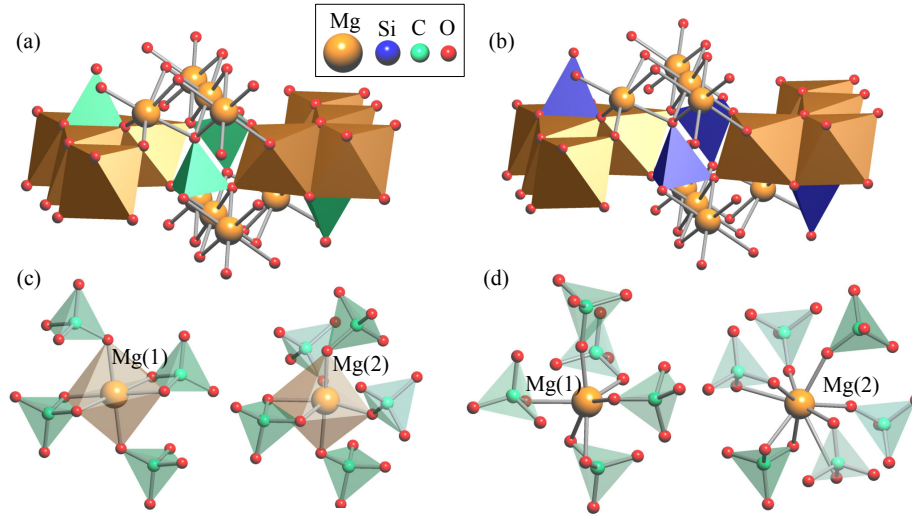


Figure 2: Comparison of crystal structures of  $\text{Mg}_2\text{CO}_4\text{-}Pnma$  (a) and  $\text{Mg}_2\text{SiO}_4\text{-}Pnma$  (b) along [010]; coordination environment around Mg(1) and Mg(2) sites in crystals structures of  $\text{Mg}_2\text{CO}_4\text{-}Pnma$  (c) and  $\text{Mg}_2\text{CO}_4\text{-}P2_1/c$  (d).

Structural data for the  $\text{Mg}_2\text{CO}_4\text{-}Pnma$  and  $\text{Mg}_2\text{CO}_4\text{-}P2_1/c$  are given in the Table 1. Both structures are dynamically stable in the investigated pressure range 0-140 GPa, and there are no imaginary frequencies in their phonon dispersion curves (Figure 3, ??). The dynamical stability of both structures at ambient pressure indicates on the possibility for their extraction from the chamber of the diamond anvil cell (DAC) after the high pressure synthesis and the further laboratory investigation. In the *Supporting information*, we have also shown phonon dispersion curves of  $\text{MgCO}_3$  and  $\text{MgO}$  (Figure S3) used for the

construction of the  $P$ - $T$  phase diagram.

Table 1:  $\text{Mg}_2\text{CO}_4$  structures introduced in the current manuscript.

| $P$ (GPa) | Space group    | Lattice parameters ( $\text{\AA}$ , deg) |                                 |                                | Atom | Coordinates |       |        |
|-----------|----------------|--|---------------------------------|--------------------------------|------|-------------|-------|--------|
|           |                |  |                                 |                                |      | x           | y     | z      |
| 50        | $Pnma$ (#62)   | $a = 8.926$<br>$\alpha = 90.0$           | $b = 5.565$<br>$\beta = 90.0$   | $c = 4.221$<br>$\gamma = 90.0$ | Mg1  | 0.000       | 0.000 | 0.500  |
|           |                |  |                                 |                                | Mg2  | 0.721       | 0.250 | 0.531  |
|           |                |  |                                 |                                | C1   | -0.097      | 0.250 | 0.087  |
|           |                |  |                                 |                                | O1   | -0.091      | 0.250 | 0.770  |
|           |                |  |                                 |                                | O2   | 0.548       | 0.250 | 0.284  |
|           |                |  |                                 |                                | O3   | 0.169       | 0.552 | 0.786  |
| 100       | $P2_1/c$ (#14) | $a = 4.408$<br>$\alpha = 90.0$           | $b = 5.383$<br>$\beta = 117.65$ | $c = 8.345$<br>$\gamma = 90.0$ | Mg1  | 0.702       | 0.360 | 0.425  |
|           |                |  |                                 |                                | Mg2  | -0.022      | 0.000 | 0.693  |
|           |                |  |                                 |                                | C1   | 0.355       | 0.282 | 0.082  |
|           |                |  |                                 |                                | O1   | 0.146       | 0.334 | 0.638  |
|           |                |  |                                 |                                | O2   | 0.681       | 0.245 | 0.197  |
|           |                |  |                                 |                                | O3   | 0.272       | 0.168 | -0.080 |
|           |                |  |                                 |                                | O4   | 0.295       | 0.520 | 0.064  |

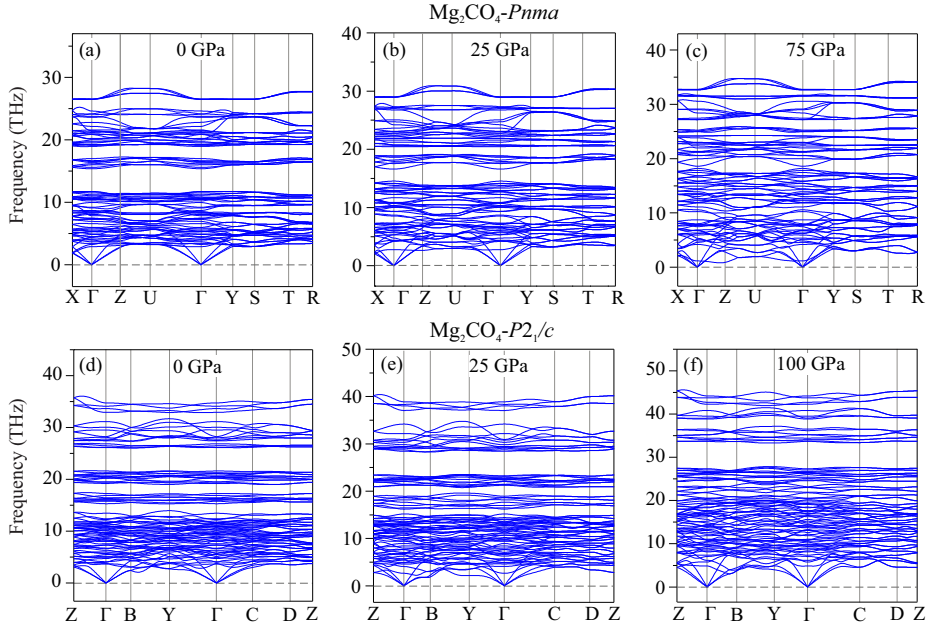


Figure 3: Phonon dispersion curves of  $\text{Mg}_2\text{CO}_4$ - $Pnma$  (a-c) and  $\text{Mg}_2\text{CO}_4$ - $P2_1/c$  (d-f) at several pressures.

There is no analogy of the found transition from  $\text{Mg}_2\text{CO}_4$ - $Pnma$  to  $\text{Mg}_2\text{CO}_4$ -

$P2_1/c$  among  $\text{Mg}_2\text{SiO}_4$  structures. However, there is one for  $\text{Ca}_2\text{SiO}_4$  structures. As  $\gamma\text{-Ca}_2\text{SiO}_4$  is isostructural to  $\text{Mg}_2\text{CO}_4\text{-}Pnma$  and  $\beta\text{-Ca}_2\text{SiO}_4$  — to  $\text{Mg}_2\text{CO}_4\text{-}P2_1/c$ , the transformation of  $\gamma\text{-Ca}_2\text{SiO}_4$  into  $\beta\text{-Ca}_2\text{SiO}_4$  realized on compression [47], is the analogue of transformation  $\text{Mg}_2\text{CO}_4\text{-}Pnma$  into  $\text{Mg}_2\text{CO}_4\text{-}P2_1/c$ . Based on the similarity of high pressure phase transitions of  $\text{Mg}_2\text{CO}_4$  and  $\text{Ca}_2\text{SiO}_4$ , the analogue of the transition  $\beta\text{-Ca}_2\text{SiO}_4 \rightarrow \alpha'_H\text{-Ca}_2\text{SiO}_4$  can be suggested. In this case, on heating,  $\text{Mg}_2\text{CO}_4\text{-}P2_1/c$  will transform into the hypothetical phase  $\text{Mg}_2\text{CO}_4\text{-}Pnma\text{-II}$ , analogue of  $\alpha'_H\text{-Ca}_2\text{SiO}_4$ . The performed calculations of phonon dispersion curves of  $\text{Mg}_2\text{CO}_4\text{-}Pnma\text{-II}$ , constructed based on the structure of  $\alpha'_H\text{-Ca}_2\text{SiO}_4$  by corresponding atomic replacements, have shown the dynamical instability of this phase (Figure S5). However, the stabilization of the structure by the factors, which are not considered in QHA can not be excluded.

### **$P$ – $T$ phase diagram**

The performed enthalpy calculations of the  $\text{Mg}_2\text{CO}_4$ ,  $\text{MgO}$ , and  $\text{MgCO}_3$  structures have shown, that both  $\text{Mg}_2\text{CO}_4\text{-}Pnma$  and  $\text{Mg}_2\text{CO}_4\text{-}P2_1/c$  lie above the energetic convex hull, i.e. they are unstable and decompose to the mixture ( $\text{MgO}+\text{MgCO}_3$ ) at 0 K (Figure S6).

However, performed calculations of the Gibbs free energies in the temperature range of 0–3000 K have shown that above some temperature  $\text{Mg}_2\text{CO}_4$  became more energetically favorable than the ( $\text{MgO}+\text{MgCO}_3$ ) mixture (Figure S7). At 20 GPa, this temperature is 2420 K, which is nearly equal to the melting temperature of magnesite ( $\text{MgCO}_3\text{-}R\bar{3}c$ ) [48] (Figure 4). With increasing the pressure the temperature of transition decreases, and at 140 GPa  $\text{Mg}_2\text{CO}_4\text{-}P2_1/c$  became more favourable than the mixture of ( $\text{MgO}+\text{MgCO}_3$ ) at temperatures higher than 1085 K. Thus, in the pressure range of 50–140 GPa,  $\text{Mg}_2\text{CO}_4$  can be synthesised at temperatures 250–1100 K higher than the corresponding temperatures of  $\text{MgCO}_3$  melting (Figure 4). It suggests the possibility for the formation of Mg-orthocarbonate in most part of the Earth's lower mantle, at pressures higher than 50 GPa.

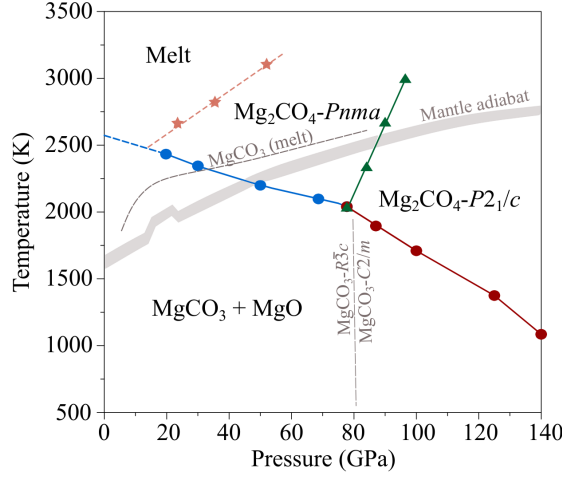


Figure 4:  $P$ - $T$  phase diagram of  $\text{Mg}_2\text{CO}_4$ . The asterisks represent calculated melting temperatures; the grey dash-dotted line — calculated phase transition boundary of  $\text{MgCO}_3$ ; the grey dashed line — melting curve of  $\text{MgCO}_3$  as reported by Solopova et al. [48]; grey solid line — mantle adiabat according to Katsura [49].

### Raman spectra

As the Raman technique is now actively used for the identification of  $sp^3$  bonded carbonates and orthocarbonates in high-pressure DAC experiments [50,51], we have calculated Raman spectra for the  $\text{Mg}_2\text{CO}_4$ - $Pnma$  phase.

The unit cells of  $\text{Mg}_2\text{CO}_4$ - $Pnma$  contain 28 atoms, i.e. there are 84 phonon modes. According to a group theoretical analysis, 36 Raman active modes are expected for  $\text{Mg}_2\text{CO}_4$ - $Pnma$ :  $\Gamma = 11A_g + 7B_{1g} + 11B_{2g} + 7B_{3g}$ . The most intense mode ( $B_{2g}$ ) corresponds to the bending and stretching vibrations in the  $[\text{CO}_4]$  tetrahedral groups and appears at  $1025 \text{ cm}^{-1}$ . The second ( $A_g$ ) and third ( $B_{1g}$ ) most intense modes appear at  $1089$  and  $1106 \text{ cm}^{-1}$ , correspondingly (Figure 5). The calculated Raman spectra at 60 GPa is shown in Figure 6.

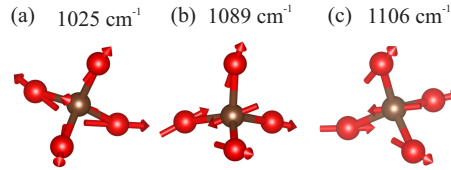


Figure 5: Displacement patterns in Raman modes of  $\text{Mg}_2\text{CO}_4$ - $Pnma$  at 60 GPa. Arrows indicate the displacements of the atoms during the specific vibration.



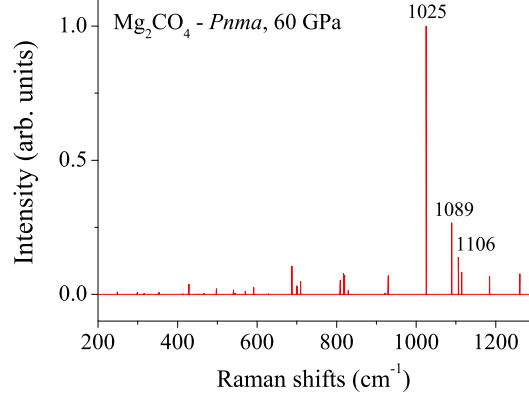


Figure 6: DFT-calculated Raman spectra of  $\text{Mg}_2\text{CO}_4$ -*Pnma* at 60 GPa.

#### Analysis of electronic denisty distribution

In both found structures, *Pnma* and *P2<sub>1</sub>/c*, four C–O bonds within  $[\text{CO}_4]$  tetrahedron are of nearly the same length. At 100 GPa, these bond distances vary in the range 1.32–1.37 Å in both structures. The similar values of bond lengths assume the covalent nature of all four bonds. The performed analysis of electron density distribution confirms this assumption. The isosurface of the electron density difference clearly shows the accumulation of charge halfway along each of the four C–O bond (Figure 7).

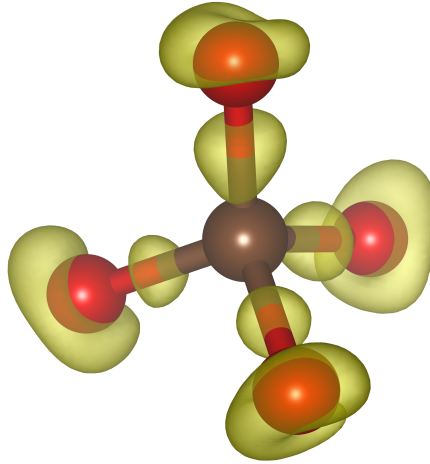


Figure 7: Isosurface of the electron density difference in  $\text{Mg}_2\text{CO}_4$ -*Pnma* structure. The isosurface shows those regions in which the electron density is larger than that obtained by overlapping electron densities of non-interacting atoms.

The isostructural character of  $\text{Mg}_2\text{CO}_4\text{-}Pnma$  and  $\text{Mg}_2\text{SiO}_4\text{-}Pnma$  gives a rare possibility for performing the comparison of electron density distribution in the structures of carbonate and silicate.

At 0 GPa, the Si–O bond is longer than C–O bond on 15–19 %. The obtained Bader charge of  $\text{C}^{4+}$  is predictably lower than that of  $\text{Si}^{4+}$ , 1.914 and 3.109 for  $\text{C}^{4+}$  and  $\text{Si}^{4+}$ , respectively. This indicates the more covalent character of C–O bond in comparison with the Si–O bond. This difference in the nature of the bonds together with the difference of atomic sizes will obstruct (Si,C) isomorphism, despite the isostructural character of orthosilicates and orthocarbonates of Mg, Ca [15], and Sr [17]. Bader charges of the other atoms are summarised in Table 2.

Table 2: Comparison of Bader charges on atoms in  $\text{Mg}_2\text{SiO}_4\text{-}Pnma$  and  $\text{Mg}_2\text{CO}_4\text{-}Pnma$  structures at 0 GPa (in unit of e).

|                           | Mg1   | Mg2   | C/Si  | O1     | O2     | O3     |
|---------------------------|-------|-------|-------|--------|--------|--------|
| $\text{Mg}_2\text{SiO}_4$ | 1.731 | 1.745 | 3.109 | -1.645 | -1.657 | -1.641 |
| $\text{Mg}_2\text{CO}_4$  | 1.724 | 1.745 | 1.914 | -1.412 | -1.340 | -1.315 |

### Melting temperature and seismic properties

To compare the melting temperatures of  $\text{MgCO}_3$  and  $\text{Mg}_2\text{CO}_4$  we have calculated the melting temperatures of  $\text{Mg}_2\text{CO}_4\text{-}Pnma$  and compare them with the experimental values of magnesite melting temperatures.

The obtained values of the  $\text{Mg}_2\text{CO}_4\text{-}Pnma$  melting temperatures at 23.7 GPa, 35.5 GPa and 52.2 GPa equal to 2661 K, 2819 K, and 3109 K, respectively (Figure S8). These values are 14–22 % higher than the experimentally measured melting temperatures of magnesite and comparable with solidi of silicate rocks under lower mantle  $P$ – $T$  conditions [52]. As can be seen from Figure 4 the difference in melting temperatures promptly increases with pressure, reaching 500 K at nearly 40 GPa.

To compare the seismic properties of  $\text{MgCO}_3$  and  $\text{Mg}_2\text{CO}_4$ , we have calculated the elastic stiffness tensor and compressional/shear sound velocities ( $V_p/V_s$ ) for  $\text{Mg}_2\text{CO}_4\text{-}Pnma$  and Mg-orthocarbonate. We have not aimed the investigation of trends for the changes of elastic properties on compression nor their description during  $Pnma \rightarrow P2_1/c$  transition, but only the rough comparison of carbonate and orthocarbonate properties. By this reason, calculations have been performed only at 50 GPa and 0 K for  $\text{Mg}_2\text{CO}_4\text{-}Pnma$  and magnesite structures.

The obtained elastic properties of  $\text{Mg}_2\text{CO}_4\text{-}Pnma$  and magnesite are summarized in Table S1 and Table S2. Obtained values of  $C_{ij}$ ,  $B$ ,  $G$ ,  $V_p$ , and  $V_s$  for magnesite are in good agreement with the previous results of theoretical calculations [53]. According to our results, the density and both bulk and shear moduli of  $\text{Mg}_2\text{CO}_4\text{-}Pnma$  are higher than that of magnesite by 4–5 %. Orthocarbonate

is similar to carbonate in sense of seismic velocities  $V_p$  and  $V_s$ , but orthocarbonate is more anisotropic, owning higher universal anisotropy ( $A^U$ ). The value of  $A^U$  for  $\text{Mg}_2\text{CO}_4\text{-}Pnma$  is 0.4772, while that for magnesite is 0.2838.

## Acknowledgments

This study was funded by the RFBR under research projects #20-03-00774 and #20-35-90043. Crystal structure predictions, calculation of  $P$ – $T$  phase diagram, Raman spectra, and electronic density distribution were performed within the project #20-03-00774, while calculations of melting curve — within the project #20-35-90043. Calculations of elastic properties were supported by a state-assigned project of the IGM SB RAS.

The computations were performed using resources provided by the Novosibirsk State University Supercomputer Center.

## References

- [1] Gavryushkin, P. N.; Behtenova, A.; Popov, Z. I.; Bakakin, V. V.; Likhacheva, A. Y.; Litasov, K. D.; Gavryushkin, A. Toward analysis of structural changes common for alkaline carbonates and binary compounds: prediction of high-pressure structures of  $\text{Li}_2\text{CO}_3$ ,  $\text{Na}_2\text{CO}_3$ , and  $\text{K}_2\text{CO}_3$ . *Crystal Growth & Design* 16, **2016**, 5612–5617.
- [2] Gavryushkin, P. N.; Bekhtenova, A.; Lobanov, S. S.; Shatskiy, A.; Likhacheva, A. Y.; Sagatova, D.; Sagatov, N.; Rashchenko, S. V.; Litasov, K. D.; Sharygin, I. S.; et al. High-pressure phase diagrams of  $\text{Na}_2\text{CO}_3$  and  $\text{K}_2\text{CO}_3$ . *Minerals* 9, **2019**, 599.
- [3] Grzechnik, A.; Bouvier, P.; Farina, L. High-pressure structure of  $\text{Li}_2\text{CO}_3$ . *Journal of Solid State Chemistry* 173, **2003**, 13–19.
- [4] Oganov, A. R.; Glass, C. W.; Ono, S. High-pressure phases of  $\text{CaCO}_3$ : Crystal structure prediction and experiment. *Earth and Planetary Science Letters* 241, **2006**, 95 – 103.
- [5] Pickard, C. J.; Needs, R. J. Structures and stability of calcium and magnesium carbonates at mantle pressures. *Physical Review B* 91, **2015**, 104101.
- [6] Gavryushkin, P. N.; Martirosyan, N. S.; Inerbaev, T. M.; Popov, Z. I.; Rashchenko, S. V.; Likhacheva, A. Y.; Lobanov, S. S.; Goncharov, A. F.; Prakapenka, V. B.; Litasov, K. D. Aragonite-II and  $\text{CaCO}_3$ -VII: New high-pressure, high-temperature polymorphs of  $\text{CaCO}_3$ . *Crystal Growth & Design* 17, **2017**, 6291–6296.
- [7] Smith, D.; Lawler, K. V.; Martinez-Canales, M.; Daykin, A. W.; Fussell, Z.; Smith, G. A.; Childs, C.; Smith, J. S.; Pickard, C. J.; Salamat, A.

- Postaragonite phases of  $\text{CaCO}_3$  at lower mantle pressures. *Physical Review Materials* **2**, **2018**, 013605.
- [8] Solomatova, N. V.; Asimow, P. D. First-principles calculations of high-pressure iron-bearing monoclinic dolomite and single-cation carbonates with internally consistent hubbard u. *Physics and Chemistry of Minerals* **2017**, 1–10.
  - [9] Binck, J.; Chariton, S.; Stekiel, M.; Bayarjargal, L.; Morgenroth, W.; Milman, V.; Dubrovinsky, L.; Winkler, B. High-pressure, high-temperature phase stability of iron-poor dolomite and the structures of dolomite-IIIc and dolomite-V. *Physics of the Earth and Planetary Interiors* **299**, **2020**, 106403.
  - [10] Merlini, M.; Cerantola, V.; Gatta, G. D.; Gemmi, M.; Hanfland, M.; Kumpen, I.; Lotti, P.; Müller, H.; Zhang, L. Dolomite-IV: Candidate structure for a carbonate in the earth’s lower mantle. *American Mineralogist* **102**, **2017**, 1763–1766.
  - [11] Fyfe, W. Lattice energies, phase transformations and volatiles in the mantle. *Physics of the Earth and Planetary Interiors* **3**, **1970**, 196–200.
  - [12] Irving, A.; Wyllie, P. Melting relationships in  $\text{CaO-CO}_2$  and  $\text{MgO-CO}_2$  to 36 kilobars with comments on  $\text{CO}_2$  in the mantle. *Earth and Planetary Science Letters* **20**, **1973**, 220–225.
  - [13] Katsura, T.; Tsuchida, Y.; Ito, E.; Yagi, T.; Utsumi, W.; Akimoto, S.-i. Stability of magnesite under the lower mantle conditions. *Proceedings of the Japan Academy, Series B* **67**, **1991**, 57–60.
  - [14] Yao, X.; Xie, C.; Dong, X.; Oganov, A. R.; Zeng, Q. Novel high-pressure calcium carbonates. *Physical Review B* **98**, **2018**, 014108.
  - [15] Sagatova, D.; Shatskiy, A.; Sagatov, N.; Gavryushkin, P. N.; Litasov, K. D. Calcium orthocarbonate,  $\text{Ca}_2\text{CO}_4$ -*Pnma*: A potential host for subducting carbon in the transition zone and lower mantle. *Lithos* **370-371**, **2020**, 105637.
  - [16] Gavryushkin, P. N.; Sagatova, D.; Sagatov, N.; Banaev, M. V. Silicate-like crystalchemistry for carbonates at high pressure. Reality or not? *IV Conference and School for Young Scientists Non-Ambient Diffraction and Nanomaterials (Book of abstracts, 19-21.10.2020)* **2020**, 38.
  - [17] Laniel, D.; Binck, J.; Winkler, B.; Vogel, S.; Fedotenko, T.; Chariton, S.; Prakapenka, V.; Milman, V.; Schnick, W.; Dubrovinsky, L.; Dubrovinskaya, N. Synthesis, crystal structure and structure–property relations of strontium orthocarbonate,  $\text{Sr}_2\text{CO}_4$ . *Acta Crystallographica Section B* **77**, **2021**, 131–137.

- [18] Binck, J.; Laniel, D.; L., B.; Khandarkhaeva, S.; Fedotenko, T.; Aslan-  
dukov, A.; Glazyrin, K.; Milman, V.; Chariton, S.; Prakapenka, V. B.;  
Dubrovinskaia, N.; Dubrovinsky, L.; Winkler, B. Synthesis of calcium or-  
thocarbonate,  $\text{Ca}_2\text{CO}_4\text{-Pnma}$ , at p,t-conditions of earth’s transition zone  
and lower mantle. *Am. Mineral.* **2021**.
- [19] Oganov, A. R.; Pickard, C. J.; Zhu, Q.; Needs, R. J. Structure prediction  
drives materials discovery. *Nature Reviews Materials* *4*, **2019**, 331–348.
- [20] Kanzaki, M. High-pressure phase relations in  $\text{Zn}_2\text{SiO}_4$  system: A first-  
principles study. *arXiv preprint arXiv:1903.05339* **2019**.
- [21] Tomioka, N.; Bindl, L.; Okuchi, T.; Miyahara, M.; Iitaka, T.; Li, Z.;  
Kawatsu, T.; Xie, X.; Purevjav, N.; Tani, R.; et al. Poirierite, a dense  
metastable polymorph of magnesium iron silicate in shocked meteorites.  
*Communications Earth & Environment* *2*, **2021**, 1–8.
- [22] Horiuchi, H.; Sawamoto, H.  $\beta\text{-Mg}_2\text{SiO}_4$ : Single-crystal X-ray diffraction  
study. *American Mineralogist* *66*, **1981**, 568–575.
- [23] Smyth, J. R.; Hazen, R. M. The crystal structures of forsterite and hortonolite  
at several temperatures up to 900 C. *American Mineralogist* *58*, **1973**,  
588–593.
- [24] Hawthorne, F. C.; Ferguson, R. B. Anhydrous sulphates; I, Refinement  
of the crystal structure of celestite with an appendix on the structure of  
thenardite. *The Canadian Mineralogist* *13*, **1975**, 181–187.
- [25] Alcock, N. W.; Evans, D. A.; Jenkins, H. D. B. Lithium sulphate – a  
redetermination. *Acta Crystallographica Section B* *29*, **1973**, 360–361.
- [26] Oganov, A. R.; Glass, C. W. Crystal structure prediction using ab initio  
evolutionary techniques: Principles and applications. *The Journal of  
Chemical Physics* *124*, **2006**, 244704.
- [27] Oganov, A. R.; Lyakhov, A. O.; Valle, M. How evolutionary crystal struc-  
ture prediction works—and why. *Accounts of Chemical Research* *44*, **2011**,  
227–237. PMID: 21361336.
- [28] Lyakhov, A. O.; Oganov, A. R.; Stokes, H. T.; Zhu, Q. New developments  
in evolutionary structure prediction algorithm uspeh. *Computer Physics  
Communications* *184*, **2013**, 1172 – 1182.
- [29] Bushlanov, P. V.; Blatov, V. A.; Oganov, A. R. Topology-based crystal  
structure generator. *Computer Physics Communications* *236*, **2019**, 1 – 7.
- [30] Pickard, C. J.; Needs, R. J. High-pressure phases of silane. *Physical Review  
Letters* *97*, **2006**, 045504.
- [31] Pickard, C. J.; Needs, R. J. Ab initio random structure searching. *Journal  
of Physics: Condensed Matter* *23*, **2011**, 053201.

- [32] Kresse, G.; Furthmüller, J. Efficient iterative schemes for ab initio total-energy calculations using a plane-wave basis set. *Physical Review B* **54**, **1996**, 11169–11186.
- [33] Kresse, G.; Furthmüller, J. Efficiency of ab-initio total energy calculations for metals and semiconductors using a plane-wave basis set. *Computational Materials Science* **6**, **1996**, 15 – 50.
- [34] Togo, A.; Tanaka, I. First principles phonon calculations in materials science. *Scripta Materialia* **108**, **2015**, 1–5.
- [35] Gavryushkin, P. N.; Sagatov, N.; Belonoshko, A. B.; Banaev, M. V.; Litasov, K. D. Disordered aragonite: The new high-pressure, high-temperature phase of  $\text{CaCO}_3$ . *The Journal of Physical Chemistry C* **124**, **2020**, 26467–26473.
- [36] Belonoshko, A. B.; Skorodumova, N. V.; Rosengren, A.; Johansson, B. Melting and critical superheating. *Physical Review B* **73**, **2006**, 012201.
- [37] Hill, R. The elastic behaviour of a crystalline aggregate. *Proceedings of the Physical Society. Section A* **65**, **1952**, 349–354.
- [38] Hill, R. Elastic properties of reinforced solids: Some theoretical principles. *Journal of the Mechanics and Physics of Solids* **11**, **1963**, 357 – 372.
- [39] Fonari, A.; Stauffer, S. *vasp\_raman.py*. <https://github.com/raman-sc/VASP/>, **2013**.
- [40] Tang, W.; Sanville, E.; Henkelman, G. A grid-based bader analysis algorithm without lattice bias. *Journal of Physics: Condensed Matter* **21**, **2009**, 084204.
- [41] Henkelman, G.; Arnaldsson, A.; Jónsson, H. A fast and robust algorithm for bader decomposition of charge density. *Computational Materials Science* **36**, **2006**, 354–360.
- [42] Stokes, H. T.; Hatch, D. M. FINDSYM: program for identifying the space-group symmetry of a crystal. *Journal of Applied Crystallography* **38**, **2005**, 237–238.
- [43] Momma, K.; Izumi, F. VESTA 3 for three-dimensional visualization of crystal, volumetric and morphology data. *J. Appl. Crystallogr.* **44**, **2011**, 1272–1276.
- [44] Blatov, V. A.; Shevchenko, A. P.; Proserpio, D. M. Applied topological analysis of crystal structures with the program package ToposPro. *Crystal Growth & Design* **14**, **2014**, 3576–3586.
- [45] Ganose, A. M.; Jain, A. Robocrystallographer: automated crystal structure text descriptions and analysis. *MRS Communications* **9**, **2019**, 874–881.

- [46] Dorogokupets, P.; Dymshits, A.; Sokolova, T.; Danilov, B.; Litasov, K. The equations of state of forsterite, wadsleyite, ringwoodite, akimotoite,  $\text{MgSiO}_3$ -perovskite, and postperovskite and phase diagram for the  $\text{Mg}_2\text{SiO}_4$  system at pressures of up to 130 GPa. *Russian Geology and Geophysics* **56**, **2015**, 172–189.
- [47] Belmonte, D.; Ottonello, G.; Zuccolini, M. V. Ab initio-assisted assessment of the  $\text{CaO-SiO}_2$  system under pressure. *Calphad* **59**, **2017**, 12 – 30.
- [48] Solopova, N. A.; Dubrovinsky, L.; Spivak, A. V.; Litvin, Y. A.; Dubrovinskaya, N. Melting and decomposition of  $\text{MgCO}_3$  at pressures up to 84 GPa. *Physics and Chemistry of Minerals* **42**, **2015**, 73–81.
- [49] Katsura, T.; Yoneda, A.; Yamazaki, D.; Yoshino, T.; Ito, E. Adiabatic temperature profile in the mantle. *Physics of the Earth and Planetary Interiors* **183**, **2010**, 212 – 218. Special Issue on Deep Slab and Mantle Dynamics.
- [50] Lobanov, S. S.; Dong, X.; Martirosyan, N. S.; Samtsevich, A. I.; Stevanovic, V.; Gavryushkin, P. N.; Litasov, K. D.; Greenberg, E.; Prakapenka, V. B.; Oganov, A. R.; et al. Raman spectroscopy and X-ray diffraction of  $\text{sp}^3$   $\text{CaCO}_3$  at lower mantle pressures. *Physical Review B* **96**, **2017**, 104101.
- [51] Binck, J.; Bayarjargal, L.; Lobanov, S. S.; Morgenroth, W.; Luchitskaia, R.; Pickard, C. J.; Milman, V.; Refson, K.; Jochym, D. B.; Byrne, P.; et al. Phase stabilities of  $\text{MgCO}_3$  and  $\text{MgCO}_3$ -II studied by Raman spectroscopy, X-ray diffraction, and density functional theory calculations. *Physical Review Materials* **4**, **2020**, 055001.
- [52] Litasov, K. D.; Shatskiy, A. Carbon-bearing magmas in the earth’s deep interior. In *Magmas Under Pressure*. Elsevier, **2018**, pages 43–82.
- [53] Li, Z.; Stackhouse, S. Iron-rich carbonates stabilized by magnetic entropy at lower mantle conditions. *Earth and Planetary Science Letters* **531**, **2020**, 115959.